

Research on Overall Aerodynamic Design of Grid-Duct Integrated Vertical Take-off and Landing (VTOL) Fixed-Wing Aircraft

Bole Li[1] & Baigang Mi[2]

[1]Northwestern Polytechnical University, Xi'an, 710072, China.
[2]Northwestern Polytechnical University, Xi'an, 710072, China.
[1]National Key Laboratory of Aircraft Configuration Design, Xi'an, 710072, China.
[2]National Key Laboratory of Aircraft Configuration Design, Xi'an, 710072, China.
[1]18980746909@163.com,[2]mibaigang@nwpu.edu.cn

Abstract

Vertical take-off and landing (VTOL) fixed-wing aircraft combine the high-speed cruise efficiency of fixed-wing aircraft with the vertical take-off and landing flexibility of multi-rotor aircraft, showing significant application potential in fields such as urban air mobility, logistics, and emergency rescue. This paper proposes a novel grid-duct integrated VTOL fixed-wing aircraft that fully leverages the multi-lifting-surface and multi-control-surface advantages of grid wings. The airfoil-equipped transverse grids replace conventional fixed wings as the primary lifting surfaces, while the propeller is positioned within the duct formed by the grid surfaces, creating a powered lift augmentation effect through grid-duct-propeller aerodynamic coupling. A comprehensive aerodynamic optimization design framework is established, encompassing: (1) Blade Element Momentum (BEM) theory-based propeller optimization for multi-condition performance balancing; (2) differentiated upper/lower grid airfoil optimization using CST parameterization and two-dimensional CFD; (3) three-dimensional aerodynamic layout optimization with multi-level CFD strategy; and (4) a rapid high-fidelity surrogate method combining BEM, actuator disk theory, and propeller wake modeling. The proposed integrated technical route provides a complete aerodynamic design solution for this novel VTOL configuration.

Keywords: VTOL; grid wing; ducted fan; aerodynamic optimization; computational fluid dynamics

Nomenclature

R Propeller radius [m]

D Propeller diameter [m]

B Number of blades

n Rotational speed [rev/s]

ω Angular velocity [rad/s]

V_∞ Freestream velocity [m/s]

ρ Air density [kg/m³]

A Disk area [m²]

J Advance ratio

C_T Thrust coefficient

C_P Power coefficient

η Propulsive efficiency

v_i Induced velocity [m/s]

W Aircraft weight [N]

T Thrust [N]

Q Torque [N·m]

P Power [W]

F Prandtl loss factor

c Chord length [m]

β Blade pitch angle [rad]

φ Inflow angle [rad]

α Angle of attack [rad]

C_l Airfoil lift coefficient

C_d Airfoil drag coefficient

C_m Airfoil pitching moment coefficient

Re Reynolds number

M_{tip} Tip Mach number

C_L Aircraft lift coefficient

C_D Aircraft drag coefficient

L/D Lift-to-drag ratio

FM Figure of merit

q Dynamic pressure [Pa]

1. General Introduction

Vertical Take-Off and Landing (VTOL) fixed-wing aircraft represent a significant development direction in aviation, combining the high-speed cruise capability of fixed-wing aircraft with the vertical take-off and landing flexibility of multi-rotor aircraft. With the rapid advancement of electric propulsion and energy storage technologies, VTOL fixed-wing aircraft have demonstrated substantial application potential in urban air mobility (UAM), express logistics, emergency rescue, and military reconnaissance [1-3].

Among various VTOL configurations, the tailsitter configuration has garnered significant attention due to its simple structure and absence of redundant VTOL conversion mechanisms [4]. Ducted fan power systems, owing to their high static thrust efficiency, low noise, and enhanced safety characteristics, are particularly suitable for tailsitter VTOL aircraft operating in complex near-ground environments [5-6].

Grid wings, as a special lifting surface configuration, offer advantages including multiple lifting surfaces, multiple control surfaces, and benign stall characteristics. They have been successfully applied in missile control and certain special aircraft [7]. However, the integration of grid wings with ducted fans for VTOL fixed-wing applications remains largely unexplored.

This paper proposes a novel grid-duct integrated VTOL fixed-wing aircraft. The core innovations include: (1) replacing conventional fixed wings with airfoil-equipped transverse grids as the primary lifting surfaces; (2) positioning the propeller within the duct formed by the grid wing surfaces, creating powered lift augmentation through aerodynamic coupling; (3) adopting a lifting-body fuselage to provide partial lift and trim capability.

However, the aerodynamic design of this novel configuration faces several unique challenges: the asymmetric influence of propeller slipstream on the upper and lower grid surfaces, the complex aerodynamic coupling between the propeller and grid wing, and the multi-variable optimization across hover, transition, and cruise flight conditions. This paper establishes a comprehensive aerodynamic design framework to address these challenges.

2. Grid-Duct VTOL Aircraft Conceptual Design

2.1 Aircraft Configuration Description

The proposed grid-duct integrated VTOL fixed-wing aircraft, illustrated in Figure 1, consists of the following primary components:

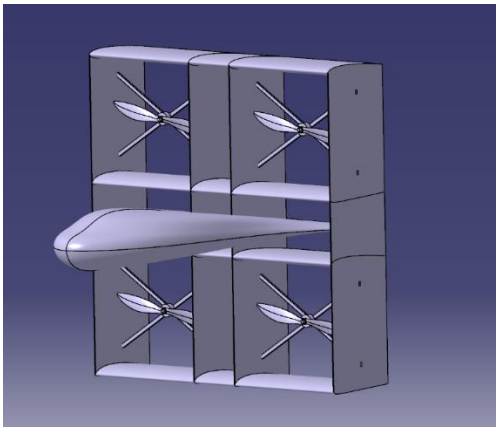


Figure 1 – Grid-duct integrated VTOL fixed-wing aircraft.

(1) Grid Lifting Surface System: The aircraft employs multiple sets of transversely arranged, airfoil-equipped grid wings as the primary lifting surfaces, replacing conventional fixed wings. Each grid wing surface is independently supported and can be equipped with trailing-edge control surfaces.

(2) Duct-Propeller Propulsion System: The propeller is positioned within the duct formed by the grid wing surfaces. Together, the grid and propeller create a specialized airflow acceleration channel. During cruise flight, the grid wing camber and installation angle naturally direct the lower-surface flow slightly downward, generating aerodynamic lift, while the propeller accelerates the internal duct airflow, further amplifying the pressure differential between the upper and lower grid surfaces — achieving powered lift augmentation.

(3) Lifting-Body Fuselage: The fuselage adopts a flattened lifting-body layout, capable of generating partial lift (approximately 15–25% of total aircraft lift) during cruise while providing pitch trim moment to reduce the required control surface deflection.

(4) Multi-Surface Control System: Leveraging the structural advantage of multiple grid lifting surfaces, independent control surfaces are separated from the grid trailing edges, providing pitch, roll, and yaw control authority. Differential propeller speed provides supplementary control during hover and transition phases.

2.2 Unique Aircraft Characteristics

Compared to conventional tailsitter VTOL fixed-wing aircraft, this configuration possesses the following distinctive characteristics:

Characteristic 1: Grid-Duct Integrated Lift System. The transverse grids, with appropriately selected airfoils, constitute the primary lifting surfaces and serve as the main lift source during level flight. The propeller and grid surfaces together form an aerodynamic acceleration duct; the propeller accelerates airflow within the duct, increasing dynamic pressure at the grid wing surfaces. The grid camber and angle of attack convert this increased dynamic pressure into lift, achieving powered lift augmentation — this is the core aerodynamic innovation of this configuration.

Characteristic 2: Powered Lift Augmentation. The propeller positioned within the grid accelerates the internal airflow velocity, further increasing the pressure differential between the upper and lower grid surfaces. This propeller-induced lift enhancement effect is a key aerodynamic feature distinguishing the grid-duct configuration from conventional designs.

Characteristic 3: Lifting-Body Fuselage Trim. The fuselage employs a lifting-body configuration, providing partial lift while contributing trimming moment, reducing the required deflection of grid control surfaces during cruise and thereby decreasing trim drag.

Characteristic 4: Compact Spanwise Dimensions. Compared to conventional tailsitter VTOL fixed-wing aircraft, the elimination of traditional high-aspect-ratio fixed wings reduces the spanwise dimensions, facilitating storage and ground operations in space-constrained environments.

2.3 Flight Profile and Mode Transition

The aircraft adopts a take-off and landing approach similar to tailsitter VTOL fixed-wing aircraft: vertical take-off followed by a pitch-over maneuver at a safe altitude to transition into fixed-wing level flight, reverse transition for landing. During the transition, the propeller slipstream must effectively cover both upper and lower grid wing surfaces to ensure continuous lift and control authority. This slipstream coverage requirement strongly couples with the propeller design and is a central constraint in the BEM optimization in Section 3. Flight profile schematic diagram is shown in Figure 2.

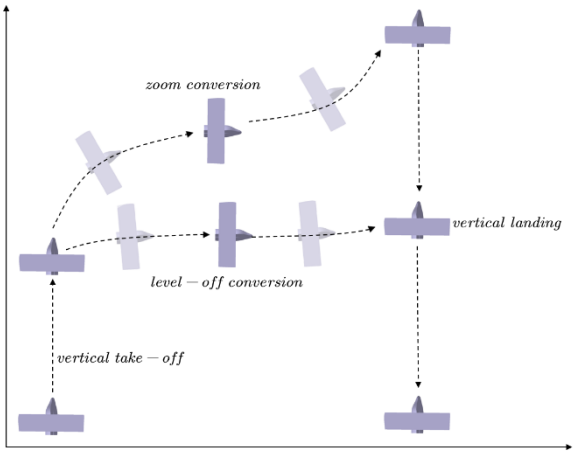


Figure 2 – Flight profile schematic diagram.

2.4 Key Aerodynamic Design Challenges

The aerodynamic design of the grid-duct VTOL fixed-wing aircraft faces the following key challenges:

Challenge 1: Asymmetric Slipstream Effects. The propeller simultaneously accelerates and redirects the airflow. For the upper grid wing, the suction effect of the propeller causes the internal duct flow to accelerate, while the outer flow remains at freestream conditions. For the lower grid wing, it experiences the propeller jet wake containing strong swirl components. The upper and lower wing surfaces operate in fundamentally different flow environments, necessitating differentiated airfoil designs.

Challenge 2: Grid Airfoil Selection and Optimization. The upper and lower grid wing surfaces operate in fundamentally different flow environments and cannot simply employ the same airfoil. The upper wing must resist lift loss under propeller suction; the lower wing must maintain high efficiency in strong slipstream. Separate optimization with distinct objective functions is required.

Challenge 3: Multi-Variable Coupled Optimization. The configuration involves multiple design variables, including grid airfoil parameters (camber, thickness, installation angle), propeller geometric parameters (blade number, chord distribution, twist distribution, pitch), propeller-grid relative position (axial, vertical, lateral), and fuselage aerodynamic shape. These variables are coupled through propeller-grid aerodynamic interaction.

3. Propeller BEM Design and Slipstream Analysis

3.1 Design Objectives and Constraints

For the grid-duct VTOL fixed-wing aircraft, the propeller cannot be designed solely for maximum isolated efficiency. Instead, the following multi-objective design requirements must be comprehensively balanced:

Objective 1: Sufficient hover thrust, satisfying $T_{hover} \geqslant k_T$, where $k_T = 1.2 \sim 1.5$ is the vertical take-off thrust margin coefficient.

Objective 2: Maximum possible cruise propulsive efficiency η_{cruise} to ensure adequate endurance and range.

Objective 3: Transition-phase slipstream that effectively covers both upper and lower grid wing surfaces, ensuring lift and control authority during mode conversion.

Objective 4: Slipstream velocity distribution, swirl intensity, and wake contraction characteristics favorable to grid lift augmentation.

Objective 5: Tip Mach number, noise level, structural loading, and motor power not exceeding engineering constraint limits.

These multi-objective requirements necessitate that the propeller achieves a comprehensive balance among hover, transition, and cruise conditions, rather than favoring any single design point.

3.2 Actuator Disk Theory Preliminary Sizing

Prior to detailed BEM design, actuator disk theory is employed for rapid estimation to establish initial ranges for propeller diameter, disk loading, and hover power. For axial inflow conditions, the fundamental relationships are:

$$V_d = V_\infty + v_i \tag{1}$$

$$V_w = V_\infty + 2v_i \tag{2}$$

where v_i is the induced velocity at the disk. The thrust-induced velocity relationship is:

$$T = 2\rho A (V_\infty + v_i) v_i \tag{3}$$

Under hover conditions ($v_\infty = 0$), the induced velocity and ideal power become:

$$v_i = \sqrt{(T/(2\rho A))} \tag{4}$$

$$P_i = T \cdot vi = T^{\frac{3}{2}}/\sqrt{(2\rho A)} \tag{5}$$

Equation (5) reveals the scaling relationship between hover power and disk loading: P_i is proportional to $T^{\frac{3}{2}}/\sqrt{A}$. This indicates that larger propeller diameter and lower disk loading yield higher hover efficiency, but may increase structural weight and cruise drag.

Wake contraction is estimated using the continuity equation:

$$A_d \cdot V_d = A_W \cdot V_W \tag{6}$$

$$R_W/R = \sqrt{V_d/V_W} \tag{7}$$

In the hover far-wake, $R_W/R = \sqrt{1/2} \approx 0.707$. This demonstrates that the propeller wake undergoes significant contraction; therefore, the axial relative position between the grid surfaces and the propeller must be carefully designed to ensure adequate slipstream coverage of the grid wings.

3.3 Blade Element Momentum Theory

BEM theory divides the blade into multiple radial segments, each treated as a two-dimensional airfoil [8-9]. Its computational efficiency and clear physical interpretation make it widely applicable to propeller preliminary and optimization design. For a blade element at radial position r, the local relative velocity is:

$$W(r) = \sqrt{(V_x(r)^2 + V_\theta(r)^2)} \tag{8}$$

where the axial and tangential velocity components are:

$$V_x(r) = V_\infty + u_x(r) \tag{9}$$

$$V_\theta(r) = \Omega_r \text{-} u_\theta(r) \tag{10}$$

The inflow angle and local angle of attack are:

$$\varphi(r) = atan\,(V_x/V_\theta) \tag{11}$$

$$\alpha(r) = \beta(r) - \varphi(r) \tag{12}$$

where $\beta(r)$ is the blade pitch angle. The element lift and drag are:

$$dL = \frac{1}{2}\rho W^2 c(r) \cdot C_l(\alpha, Re) \cdot dr \tag{13}$$

$$dD = \frac{1}{2}\rho W^2 c(r) \cdot C_d(\alpha, Re) \cdot dr \tag{14}$$

Projecting lift and drag into thrust and torque directions:

$$dT = B \cdot (dL \cdot cos\varphi - dD \cdot sin\varphi) \tag{15}$$

$$dQ = B \cdot r \cdot (dL \cdot sin\varphi + dD \cdot cos\varphi) \tag{16}$$

Integration yields total thrust, torque, and power:

$$T = \int dT;\quad Q = \int dQ;\quad P = \Omega \cdot Q \tag{17-19}$$

$$T = \int dT \tag{17}$$

$$Q = \int dQ \tag{18}$$

$$P = \Omega \cdot Q \tag{19}$$

3.4 Tip and Hub Loss Corrections

Finite blade count induces tip leakage and induced losses, corrected using the Prandtl tip loss factor:

$$F_{tip} = (\frac{2}{\pi}) \cdot acos\left(e^{\frac{-B(R-r)}{2r \cdot \sin\varphi}}\right) \tag{20}$$

$$F_{hub} = (\frac{2}{\pi}) \cdot acos\left(e^{\frac{-B(r-r_h)}{2r_h \cdot \sin\varphi}}\right) \tag{21}$$

$$F = F_{tip} \cdot F_{hub} \tag{22}$$

The BEM momentum equation is corrected to:

$$dT_{momentum} = 4\pi r \rho {V_\infty}^2 a(1+a) F dr \tag{23}$$

where $a = \frac{v_i}{V_\infty}$. For hover or low-speed transition conditions (V_∞ approaching 0), this formulation encounters numerical singularity; in such cases, an alternative formulation based on disk-plane thrust coefficient is employed to ensure solver robustness.

3.5 Propeller Optimization Design Procedure

The propeller optimization design procedure established in this paper is as follows:

Step 1: Define design conditions. At minimum, three conditions are set: Condition A (hover, $V_\infty = 0$), Condition B (transition, low V_∞, high α_{body}), Condition C (cruise, $V_\infty = V_{cruise}$). Each condition is assigned a weight factor based on mission requirements.

Step 2: Determine disk area from hover thrust requirement. Single propeller hover thrust:

$$T_{\mathrm{single}} \geqslant \frac{k_T \cdot W}{N_{prop}} \tag{24}$$

Disk area: $A = \frac{T_{\mathrm{single}}}{2\rho {v_i}^2}$;

Step 3: Determine rotational speed and tip speed constraints. Tip Mach number:

$$M_{tip} = \frac{\Omega R}{a_{sound}} < 0.55 \sim 0.65 \tag{25}$$

to control noise and compressibility losses.

Step 4: Select blade count, pitch, and initial twist distribution. The local optimum pitch angle is:

$$\beta(r) = \varphi(r) + \alpha_{opt}(r) \tag{26}$$

where α_{opt} is the angle of attack corresponding to maximum $\frac{C_l}{C_d}$ for the selected airfoil at the local Reynolds number.

Step 5: BEM iterative optimization. Design variables: $c(r)$, $\beta(r)$, $airfoil(r)$, B, R, n. The optimization problem is formulated as: minimize {P_{hover}, $-\eta_{cruise}$, slipstream non-uniformity, torque ripple, M_{tip}}.

Step 6: Output slipstream distribution. The BEM solution provides $u_{x(r,z)}$, $u_{\theta(r,z)}$, $R_{w(z)}$, $q_{slip(r,z)}$, and $\alpha_{induced}$ fields, which are directly transferred to subsequent airfoil optimization and three-dimensional CFD analyses.

4. Two-Dimensional CFD Airfoil Aerodynamic Optimization

4.1 Necessity of Separate Upper and Lower Airfoil Optimization

In the grid-duct configuration, the upper and lower grid wing surfaces operate in fundamentally different flow environments. As shown in Figure 3, the upper wing experiences the combined effects of propeller suction, local acceleration, and decreased static pressure; the lower wing experiences strong propeller jet slipstream with increased dynamic pressure and swirl. These asymmetric flow conditions necessitate separate optimization of the upper and lower wing airfoils.

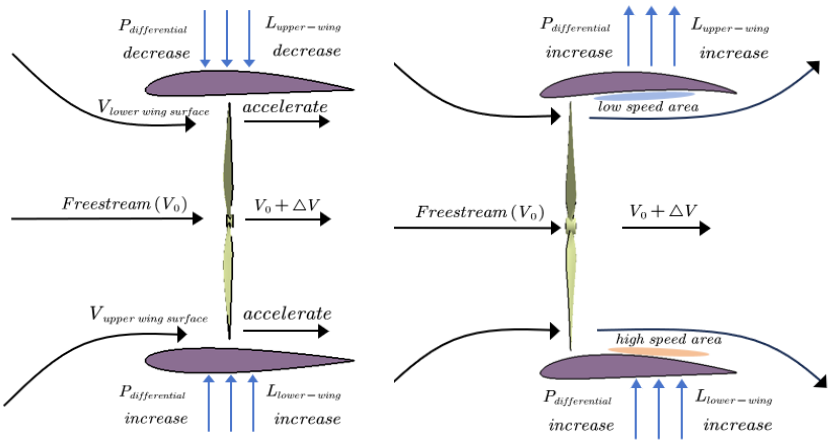


Figure 3 – Grid airfoil aerodynamic optimization schematic diagram.

The design logic is: the upper grid wing employs a high-camber, high-lift, separation-resistant airfoil design; the lower grid wing employs a moderate-camber, high-efficiency, low-drag, low-pitching-moment airfoil design, so that the combined lift increment and trim moment of both wing surfaces are optimized simultaneously.

4.2 Local Effective Inflow Modeling

From the propeller slipstream results of Section 3, the local effective velocity at each grid wing surface is established:

$$V_{eff} = \sqrt{\left[(V_\infty + u_x)^2 + u_\theta{}^2 + u_z{}^2 \right]} \tag{27}$$

The effective angle of attack is:

$$\alpha_{eff} = \alpha_{body} + i_{wing} + \Delta\alpha_{slipstream} \tag{28}$$

$$\Delta\alpha_{slipstream} = atan\left(\frac{u_z}{V_\infty + u_x}\right) \tag{29}$$

Local Reynolds number and dynamic pressure:

$$\mathrm{Re} = \frac{\rho \cdot V_{eff} \cdot c_g}{\mu} \tag{30}$$

$$q_{eff} = \frac{1}{2}\rho \cdot V_{eff}{}^2 \tag{31}$$

Airfoil optimization must be conducted under multiple Re and α_{eff} combinations through multi-condition evaluation, rather than targeting only a single cruise Reynolds number design point.

4.3 Airfoil Parameterization Method

The CST (Class-Shape Transformation) parameterization method is adopted to describe airfoil geometry [10]:

$$y(x)/c = C(x) \cdot S(x) + x \cdot \Delta z_{TE}/c \tag{32}$$

where the class function $C(x) = x^{N_1} \cdot (1\text{-}x)^{N_2}$, and the shape function $S(x)$ is represented by a linear combination of Bernstein polynomial basis functions. The design variables A_i separately control the upper and lower surface geometries. The advantages of CST parameterization include: geometrically continuous and smooth surfaces, a controllable number of design variables (typically 5–8 per surface), convenient constraint of leading-edge radius and trailing-edge angle, and good intuitive correspondence between design variables and geometric features.

4.4 Upper Grid Airfoil Optimization

The upper wing is susceptible to lift loss due to propeller suction and local pressure variations. Therefore, the upper wing optimization objective is 'high lift + separation resistance + moderate moment.' Upper wing design variables: $camber_{upper}$, $\frac{t}{c}$, $x_{t\max}$, $x_{camber-\max}$, $leading_{edge-radius}$, $trailing_{edge-angle}$, installation angle i_{upper}, $flap_{ratio}$ f.

The optimization objective function is formulated as:

$$maximizeJupper = w_1 \cdot \left(\frac{C_l}{C_d}\right)_{cruise} + w_2 \cdot C_{l,transition} + w_3 \cdot stall_m argin - w_4 \cdot |C_m - C_{m,target}| - w_5 \cdot separatio_{npenalty} \quad (33)$$

Constraints: $C_d \leq C_{d\max}$; $C_{m\min} \leq C_m \leq C_{m\ \max}$; $\frac{t}{c} \geq t_{\min/c}$; separation location $x_{sep} \geq x_{sep\ \min}$; $C_{l\ transition} \geq C_{l\ required}$.

Upper wing design guidelines: adopt substantial camber to enhance low-angle-of-attack lift; moderately increase leading-edge radius to improve high-angle-of-attack stall resistance; avoid excessively rearward maximum thickness position to prevent abrupt trailing-edge stall at high angles of attack.

4.5 Lower Grid Airfoil Optimization

The lower wing operates in a stronger accelerated slipstream with higher dynamic pressure. While lift naturally increases, drag and moment also increase accordingly. Therefore, the lower wing optimization objective is 'efficiency + trim + control effectiveness.' The optimization objective function is:

$$maximizeJ_{lower} = w_1 \cdot \left(\frac{C_l}{C_d}\right)_{powered} + w_2 \cdot control_{effectiveness} + w_3 \cdot C_{m\ stability} - w_4 \cdot drag_{rise} - w_5 \cdot separation_{penalty} \quad (34)$$

Constraints: $C_{d\ powered} \leq C_{d\lim it}$; $|C_m| \leq C_{m\lim it}$; $dC_l/d\alpha \geq min_{slope}$; $dC_m/d\delta_e \geq min_{control-authority}$.

Lower wing design guidelines: employ moderate rather than extreme camber; position maximum thickness at 30–40% chord to avoid trailing-edge separation; maintain high C_l/C_d under elevated dynamic pressure; provide adequate control derivative $dC_m/d\delta_e$ to ensure pitch control authority.

4.6 Two-Dimensional CFD Computational Procedure

Step 1: Establish airfoil sample library. Initial airfoils are selected from low-Reynolds-number airfoil databases, referencing UIUC low-speed airfoil experimental data [11] and NASA low-Reynolds-number airfoil experimental data [12].

Step 2: XFOIL/MSES rapid screening. XFOIL [13] is employed to compute $C_l - \alpha$, $C_d - \alpha$, $C_m - \alpha$, C_l/C_d, and transition location, eliminating airfoils exhibiting premature stall, excessive drag, or excessive pitching moment.

Step 3: Two-dimensional RANS high-fidelity computation. Candidate airfoils are analyzed using the SST k-ω turbulence model with γ-Re_θ transition model. Grid requirements: $y^+ \approx 1$, far-field boundary > 50c, total grid points approximately 80,000–120,000.

Step 4: Multi-condition airfoil optimization. Airfoil performance is evaluated at minimum under the following conditions: cruise (no strong slipstream), transition (strong slipstream), hover/low-speed (maximum angle of attack).

Step 5: Combined upper-lower wing evaluation. A combined metric serves as the final selection criterion:

$$J_{grid} = W_1 \cdot (L/D)_{grid} + W_2 \cdot C_{l,total,transition} + W_3 \cdot control_{margin} - W_4 \cdot |C_{m,total} - C_{m,trim}| - W_5 \cdot interference_{drag} \quad (35)$$

5. Three-Dimensional CFD Aerodynamic Layout Optimization

5.1 Necessity of Three-Dimensional Optimization

Two-dimensional airfoil optimization addresses the question of 'how well does this airfoil perform under a given equivalent inflow,' but cannot resolve the following critical three-dimensional issues: propeller-grid axial and vertical relative positioning, three-dimensional slipstream-grid interaction (spanwise non-uniformity), finite-span three-dimensional effects (tip vortices, induced drag), duct/endplate/side-plate three-dimensional effects, fuselage-grid aerodynamic interference, and multi-propeller wake interaction and superposition. These issues make three-dimensional layout optimization an indispensable step in the overall aerodynamic design.

5.2 Three-Dimensional Design Variables

The three-dimensional optimization encompasses the following primary design variables: D/R (propeller diameter/radius); x_p/c (propeller axial position relative to grid wing); z_p/h (propeller vertical position within the duct); grid span and chord; duct/endplate geometry parameters; fuselage-grid gap and fairing shape; and control surface span and chord ratios. These variables are coupled and must be optimized simultaneously.

5.3 Three-Dimensional Performance Metrics

A multi-dimensional evaluation metric system is established:

aerodynamic efficiency: $L/D = C_L/C_D$; $P_L = T/P$

hover performance: $FM = T^{3/2}/(P \cdot \sqrt{(2\rho A)})$

thrust augmentation: $K_{T-aug} = T_{grid-ducted}/T_{open-prop}$

slipstream utilization： $\eta_{slip} = \int (q_{slip} dS)_{grid} / \int (q_{slip} dA)_{disk}$

The comprehensive objective function is:

$$\begin{aligned} maximize J_{3D} = w_1 \cdot (L/D)_{cruise} + w_2 \cdot FM_{hover} + w_3 \cdot K_{T_{aug}} + w_4 \cdot control_{margin} \\ - w_5 \cdot trim_{power} - w_6 \cdot separation_{volume} - w_7 \cdot moment_{coupling} \end{aligned} \quad (36)$$

5.4 Multi-Level CFD Computational Strategy

To balance computational cost and accuracy, a three-level CFD computational hierarchy is adopted:

Level 1: Actuator Disk Rapid CFD. The rotating blades are replaced with momentum source terms:

$$S_x = (1/\Delta V_{cell}) \cdot dT \quad (37)$$

$$S_\theta = (1/\Delta V_{cell}) \cdot dQ/r \quad (38)$$

This method features simple meshing (no blade surface mesh), fast computation (~5–10 minutes per case), and provides adequate accuracy for slipstream mean flow prediction, suitable for optimization iterations.

Level 2: Actuator Line / BEM-Body Force CFD. Each blade is modeled as a rotating line source, preserving blade azimuthal effects and non-uniform loading distribution, providing higher accuracy than the actuator disk method with computational cost approximately 2–5 times that of Level 1.

Level 3: MRF/Sliding Mesh High-Fidelity CFD. Only the final 3–5 optimal configurations undergo Multiple Reference Frame (MRF) or sliding mesh unsteady computation, incorporating real blade geometry modeling for final verification. This level resolves detailed flow features including blade boundary layers, tip vortices, and propeller-grid unsteady interaction, with computational cost approximately 50–200 times that of Level 1.

5.5 Three-Dimensional Optimization Procedure

Step 1: Parametric CAD automated modeling. A parametric geometric model is established, automatically generating upper and lower grid wings, propeller disk or actual blade geometry, duct/endplate/side-plates, lifting-body fuselage, and control surfaces.

Step 2: DOE sample generation. Latin Hypercube Sampling or Sobol sequences are employed to generate 100–300 design samples uniformly covering the design space.

Step 3: Actuator Disk CFD batch computation. Performance metrics are obtained, including $C_L, C_D, C_m, T, Q, P, FM, K_{T-aug}$, slipstream coverage ratio, separated flow volume, and control surface effectiveness.

Step 4: Surrogate model construction. Kriging models (Gaussian Process regression) or Radial Basis Function (RBF) networks are employed to establish surrogate mappings from design variables to performance metrics.

Step 5: Multi-objective optimization. NSGA-II (Non-dominated Sorting Genetic Algorithm II) or MOEA/D (Multi-objective Evolutionary Algorithm based on Decomposition) [16] is employed to obtain the Pareto front.

Step 6: High-fidelity re-computation and validation. The 5–10 candidate configurations on the Pareto front undergo MRF or sliding mesh high-fidelity CFD computation. Results are compared against actuator disk results; if the relative error between the surrogate model optimum and high-fidelity CFD exceeds the threshold, the surrogate model is updated and optimization is iterated.

6. Rapid High-Fidelity Surrogate Computational Method

6.1 Overall Method Architecture

To address the prohibitive computational cost of performing real-blade sliding mesh CFD in every optimization iteration, this paper proposes a rapid high-fidelity surrogate method combining BEM, actuator disk theory, and propeller wake modeling. The core data flow of this method is: BEM → obtain dT/dr, dQ/dr, $\Gamma(r)$ → Actuator Disk Theory → obtain mean induced velocity, pressure jump, wake contraction → Propeller Wake Model → obtain helical wake geometry and induced velocity field → Grid Wing Aerodynamic Model → obtain grid loading distribution → feedback to update propeller inflow → iterate to convergence.

6.2 BEM Output of Blade Loading

From the BEM computation described in Section 3, the radial distributions dT/dr, dQ/dr, $C_l(r)$, $C_d(r)$, $\alpha(r)$, and $Re(r)$ are obtained. The bound circulation is derived from the Kutta-Joukowski theorem:

$$L'(r) = \rho \cdot W(r) \cdot \Gamma(r) \quad (39)$$

$$\Gamma(r) = L'(r)/(\rho W) = \frac{1}{2} \cdot W \cdot c(r) \cdot C_l(r) \quad (40)$$

This circulation distribution constitutes the core input to the wake model.

6.3 Actuator Disk Correction for Mean Induced Velocity

For an annular element on the propeller disk:

$$dA = 2\pi r \cdot dr \tag{41}$$

$$dT = 2\rho \cdot dA \cdot (V_\infty + vi) \cdot vi \tag{42}$$

Solving yields the annular induced velocity v_i(r). The pressure jump and tangential momentum source are:

$$\Delta p(r) = dT/dA \tag{43}$$

$$\Delta \tau(r) = dQ/dA \tag{44}$$

These can be incorporated as equivalent body force source terms in CFD or potential flow/VLM models:

$$f_x(r) = \Delta p(r)/\Delta x \tag{45}$$

$$f_\theta(r) = \Delta \tau(r)/(r \cdot \Delta x) \tag{46}$$

6.4 Propeller Wake Model

The wake of each blade is approximated as a helical vortex:

$$\theta(z) = \theta_0 + \Omega \cdot z/V_w \tag{47}$$

$$p_{wake} = 2\pi \cdot V_w/\Omega \tag{48}$$

Wake radius contraction along the axial direction:

$$R_w(z) = R \cdot \sqrt{\frac{Vd}{V_w(z)}} \tag{49}$$

For higher-fidelity computation, individual trailing vortices can be released from each radial bound circulation $\Gamma(r)$. The trailing vortex strength is:

$$d\Gamma_{trailing} = -(d\Gamma_{bound}/dr) \cdot dr \tag{50}$$

The induced velocity is computed using the regularized Biot-Savart formula:

$$u(x) = \Gamma/(4\pi) \cdot \int [dl \times (x-r)/(|x-r|^2 + \varepsilon^2)^{\frac{3}{2}}] \tag{51}$$

where ε is the vortex core radius, introduced to avoid numerical singularity. The core radius can evolve with time/distance:

$$\varepsilon(z) = \sqrt{(\varepsilon_0{}^2 + 4\nu t \cdot z/V_w)} \tag{52}$$

This represents viscous dissipation of the wake using an empirical vortex core diffusion model. Goldstein's classical helical vortex theory [17] demonstrates that the optimal circulation distribution for minimum induced loss corresponds to a constant-pitch helical wake with uniform axial displacement velocity.

6.5 Coupling with Grid Wing Aerodynamics

For each aerodynamic evaluation point on the grid wing surfaces:

$$V_{local} = V_\infty + u_{momentum_disk} + u_{wake} + u_{wing_induced} \quad (53)$$

$$V_{local} = V_\infty + u_{momentum-disk} + u_{wake} + u_{wing,nduced} \tag{53}$$

The local angle of attack is:

$$\alpha_{local} = \alpha_{body} + i_{wing} + atan(w_{local}/u_{local}) \tag{54}$$

Local airfoil aerodynamic forces are obtained by interpolation from the two-dimensional airfoil database:

$$dL = \frac{1}{2}\rho \cdot V_{local}{}^2 \cdot c \cdot C_l(\alpha_{local}, Re_{local}) \cdot dy \tag{55}$$

$$dD = \frac{1}{2}\rho \cdot V_{local}{}^2 \cdot c \cdot C_d(\alpha_{local}, Re_{local}) \cdot dy \tag{56}$$

6.6 Iterative Solution Procedure

1. Input propeller geometry, grid geometry, and flight state parameters.
2. Execute BEM solution to obtain dT/dr, dQ/dr, $\Gamma(r)$.
3. Actuator disk theory solution for $v_i(r)$, $\Delta p(r)$, $R_w(z)$.
4. Generate propeller wake geometry and compute the induced velocity field.
5. Superimpose induced velocities onto upper and lower grid wing surface evaluation points.
6. Compute grid wing loading based on the two-dimensional airfoil polar curve database.
7. Feed back grid-wing-induced velocities to the propeller inflow boundary condition.
8. Re-solve BEM with updated inflow.
9. Iterate until convergence.

Convergence criteria:

$$|T_k\text{-}T_{k\text{-}1}|/T_k < 1\% \tag{57}$$

$$|Q_k\text{-}Q_{k\text{-}1}|/Q_k < 1\% \tag{58}$$

$$|C_{L,k}\text{-}C_{L,k\text{-}1}| < 0.005 \tag{59}$$

$$|C_{m,k}\text{-}C_{m,k\text{-}1}| < 0.002 \tag{60}$$

6.7 Method Advantages and Applicability

Compared to real-blade sliding mesh CFD, this method preserves multiple critical physical mechanisms: BEM preserves blade radial loading distribution; actuator disk theory preserves axial acceleration and wake contraction; the propeller wake model preserves swirl and helical vortex structure. With a computational cost of approximately 5–20 seconds per case (three orders of magnitude faster than sliding mesh CFD), this method is suitable as: the primary computational engine for optimization iterations, a rapid generator of surrogate model training data, a pre-screening tool prior to three-dimensional CFD, and a real-time performance evaluation module for flight simulation.

7. Integrated Technical Route and Conclusions

7.1 Recommended Integrated Technical Route

Synthesizing the content of all preceding sections, the recommended integrated technical route is as follows:

1. Actuator disk theory: determine initial propeller diameter, disk loading, and hover power ranges.
2. BEM optimization: optimize propeller chord distribution, twist distribution, pitch, and rotational speed.
3. Extract slipstream data: u_x, u_θ, R_{wake}, q_{slip} fields.
4. Two-dimensional airfoil optimization: separately optimize upper and lower grid wing airfoils based on local inflow conditions.
5. Establish upper and lower grid wing airfoil aerodynamic performance database.
6. Employ the BEM + Actuator Disk + Wake Method for rapid propeller-grid coupled performance computation.
7. Conduct three-dimensional parametric layout optimization.
8. Perform Actuator Disk CFD verification for Pareto-front candidate configurations.
9. Conduct MRF/Sliding Mesh high-fidelity CFD confirmation for the final selected configuration.
10. Model correction through bench testing, wind tunnel testing, or scaled flight testing.

The core principle of this technical route is: Sections 2–3 address ‘how the propeller generates appropriate slipstream,’ Section 4 addresses ‘how the upper and lower grid wings efficiently utilize this slipstream,’ Sections 5–6 address ‘how the complete aircraft achieves optimal aerodynamic performance.’ This layered decomposition of the aerodynamic design problem systematically resolves the complex coupling among propeller, grid wing, and fuselage.

7.2 Main Conclusions

This paper has established a comprehensive overall aerodynamic design framework for the novel grid-duct integrated VTOL fixed-wing aircraft, spanning propeller design, two-dimensional airfoil optimization, three-dimensional layout optimization, and rapid surrogate methods. The main conclusions are as follows:

(1) The proposed grid-duct VTOL fixed-wing aircraft configuration integrates the advantages of tailsitter aircraft (simple structure, high reliability, favorable economics) with those of ducted aircraft (high hover efficiency, low noise, enhanced safety). The grid-duct integrated design achieves powered lift augmentation through propeller-grid aerodynamic coupling, and compact spanwise dimensions through the elimination of traditional high-aspect-ratio fixed wings.

(2) Propeller design must comprehensively balance hover thrust, cruise efficiency, and transition-phase slipstream coverage across three operating conditions, rather than favoring a single design point. BEM-based multi-condition optimization provides an effective solution for this multi-objective design problem.

(3) The upper and lower grid wing surfaces require separate optimization — the upper wing employing a high-camber, high-lift, separation-resistant airfoil, and the lower wing employing a moderate-camber, high-efficiency, low-pitching-moment airfoil. The CST parameterization combined with multi-condition 2D CFD optimization provides a systematic approach.

(4) Three-dimensional layout optimization is a necessary approach for resolving the propeller-grid-duct aerodynamic coupling problem. The Actuator Disk → Actuator Line → Sliding Mesh three-level CFD strategy effectively balances computational cost and accuracy.

(5) The proposed BEM + Actuator Disk Theory + Propeller Wake Model rapid surrogate method significantly enhances optimization iteration efficiency while preserving essential physical mechanisms, and can serve as the computational engine for iterative optimization, surrogate model training, solution pre-screening, and real-time simulation.

(6) The technical feasibility of this novel grid-duct configuration has been preliminarily validated, with propeller-grid coupled thrust augmentation showing significant potential, laying a theoretical and methodological foundation for subsequent detailed design and experimental validation.

7.3 Future Outlook

Future work will focus on the following aspects: (1) conducting scaled-model wind tunnel tests to validate numerical simulation results; (2) performing unsteady CFD simulation of the flight mode transition process; (3) investigating structural dynamics characteristics of the grid wing duct under propeller excitation; (4) developing flight control systems adapted to the multi-control-surface characteristics; and (5) verifying and refining the design framework through sub-scale flight demonstrators.

8.Contact Author Email Address

mailto: 18980746909@163.com

9. Acknowledgement

The authors would like to acknowledge the support of Natural Science Foundation of Chongqing (GrantNo.CSTB2023NSCQ-MSX0042).

10.Copyright Statement

The authors confirm that they, and/or their company or organization, hold copyright on all of the original material included in this paper. The authors also confirm that they have obtained permission, from the copyright holder of any third party material included in this paper, to publish it as part of their paper. The authors confirm that they give permission, or have obtained permission from the copyright holder of this paper, for the publication and distribution of this paper as part of the ICAS 2026 proceedings or as individual off-prints from the proceedings.

References

[1] Finger D F, Braun C and Bil C. A review of configuration design for distributed propulsion transitioning VTOL aircraft. Proc Asia-Pacific International Symposium on Aerospace Technology, Seoul, Korea, 2018.

[2] Bacchini A and Cestino E. Electric VTOL configurations comparison. Aerospace, Vol. 6, No. 3, pp 26, 2019.

[3] Saeed A S, Younes A B, Cai C and Cai G. A survey of hybrid unmanned aerial vehicles. Progress in Aerospace Sciences, Vol. 98, pp 91–105, 2018.

[4] Wang Z, He C and Zhao S. Development of ducted fan tailsitter VTOL UAV: A review. Aerospace Science and Technology, Vol. 115, 106842, 2021.

[5] Pereira J L. Hover and wind-tunnel testing of shrouded rotors for improved micro air vehicle design. PhD Thesis, University of Maryland, 2008.

[6] Ko A, Ohanian O J and Gelhausen P. Ducted fan UAV modeling and simulation in preliminary design. AIAA Modeling and Simulation Technologies Conference, Hilton Head, SC, AIAA 2007-6375, 2007.

[7] Burkhalter J E and Hartfield R J. Grid fins for missile applications. Journal of Spacecraft and Rockets, Vol. 30, No. 5, pp 617–623, 1993.

[8] Adkins C N and Liebeck R H. Design of optimum propellers. Journal of Propulsion and Power, Vol. 10, No. 5, pp 676–682, 1994.

[9] Glauert H. The Elements of Aerofoil and Airscrew Theory. 2nd edition, Cambridge University Press, 1947.

[10] Kulfan B M. Universal parametric geometry representation method. Journal of Aircraft, Vol. 45, No. 1, pp 142–

158, 2008.

[11] Deters R W. Performance and slipstream characteristics of small-scale propellers at low Reynolds numbers. PhD Thesis, University of Illinois at Urbana-Champaign, 2014.

[12] McGhee R J, Walker B S and Millard B F. Experimental results for the Eppler 387 airfoil at low Reynolds numbers in the Langley low-turbulence pressure tunnel. NASA Technical Memorandum 4062, 1988.

[13] Drela M. XFOIL: An analysis and design system for low Reynolds number airfoils. Low Reynolds Number Aerodynamics, Springer, pp 1–12, 1989.

[14] Langtry R B and Menter F R. Correlation-based transition modeling for unstructured parallelized computational fluid dynamics codes. AIAA Journal, Vol. 47, No. 12, pp 2894–2906, 2009.

[15] Sorensen J N and Shen W Z. Numerical modeling of wind turbine wakes. Journal of Fluids Engineering, Vol. 124, No. 2, pp 393–399, 2002.

[16] Deb K, Pratap A, Agarwal S and Meyarivan T. A fast and elitist multiobjective genetic algorithm: NSGA-II. IEEE Transactions on Evolutionary Computation, Vol. 6, No. 2, pp 182–197, 2002.

[17] Goldstein S. On the vortex theory of screw propellers. Proceedings of the Royal Society of London, Series A, Vol. 123, No. 792, pp 440–465, 1929.

[18] Li Q, Lu H and Deng S. Validation of an actuator disk model for numerical simulation of propeller-wing interaction. Aerospace Science and Technology, Vol. 108, 106370, 2021.

[19] Cao Y, Wang Y and Zhang X. Aerodynamic analysis of distributed propulsion with actuator disk method. Aerospace, Vol. 10, No. 2, pp 172, 2023.